Author Manuscript

Author Manuscript

Author Manuscript

Author Manuscript

HHS Public Access

Author manuscript

Magn Reson Med. Author manuscript; available in PMC 2019 April 01.

Published in final edited form as:

Magn Reson Med. 2018 April ; 79(4): 1972–1980. doi:10.1002/mrm.26854.

Visualization of macrophage recruitment in head and neck carcinoma model using fluorine-19 magnetic resonance imaging

Aman Khurana[1], **Fanny Chapelin**[2], **Hongyan Xu**[1], **Joseph R. Acevedo**[3], **Alfred Molinolo**[4], **Quyen Nguyen**[5], and **Eric T. Ahrens**[1,*]

[1]Department of Radiology, University of California San Diego, CA, USA

[2]Department of Bioengineering, University of California San Diego, CA, USA

[3]School of Medicine, University of California San Diego, CA, USA

[4]Department of Pathology, University of California San Diego, CA, USA

[5]Department of Head and Neck Surgery, University of California San Diego, CA, USA

Abstract

Purpose—To evaluate the role of infiltrating macrophages in murine models of single and double mutation head and neck tumors using a novel fluorine-19 (^{19}F) MRI technology.

Methods—Tumor cell lines single-hit/SCC4 or double-hit/Cal27, with mutations of TP53 and TP53 & FHIT, respectively, were injected bilateral into flanks of (N=10) female mice. With tumors established, perfluorocarbon (PFC) nanoemulsion was injected intravenously, which labels in situ predominantly monocytes and macrophages. Longitudinal spin-density weighted ^{19}F MRI data enabled quantification of the macrophage burden in tumor and surrounding tissue.

Results—The average number of ^{19}F atoms within the tumors was twice as high in the Cal27 group compared to SCC4 (3.9×10^{19} and 2.0×10^{19} ^{19}F/tumor, respectively, $p = 0.0034$) two days post-contrast injection, signifying increased tumor associated macrophages in double-hit tumors. The difference was still significant ten days post-injection. Histology stains correlated with in vivo results, exhibiting numerous PFC labeled-macrophages in double-hit tumors and to a lesser extent in single-hit tumors.

Conclusion—This study helps establish ^{19}F MRI as a method for quantifying immune cells in the tumor microenvironment allowing distinction between double- and single-hit head and neck tumors. This technique would be extremely valuable in the clinic for pre-treatment planning, prognostics and post-treatment surveillance.

Keywords

Head and neck cancer; inflammation; MRI; fluorine-19; perfluorocarbon

[*]Corresponding Author: Eric T. Ahrens, University of California, San Diego, 9500 Gilman Dr. #0695, La Jolla, CA 92093-0695, Phone: (858) 246-0279, eta@ucsd.edu.

Author Manuscript Author Manuscript Author Manuscript Author Manuscript

Introduction

Head and neck squamous cell carcinoma (HNSCC) is a source of significant morbidity and mortality worldwide. Risk factors include human papillomavirus (HPV) status and tobacco/alcohol use (1,2). Current staging and clinical management of HNSCC patients are based on anatomic location, size, and metastatic spread (3). If patients undergo surgical excision without adjuvant therapy, management decisions are guided by lymph node invasion or presence/absence of bone invasion (4). Patients with locally advanced disease are treated aggressively with multimodal therapy including chemotherapy and radiotherapy along with surgical resection (5).

HPV is increasingly responsible for the growing incidence of oropharyngeal squamous cell carcinoma, representing 30% of HNSCC tumors (6). HPV-positive tumor status is usually associated with better response to therapy and survival and is currently the strongest prognostic factor for these patients (7). For HPV-negative tumors, no prognostic assays are widely accepted (4). We designed this project based on the findings of our prior work (8) querying The Cancer Genomic Atlas (TCGA) (7), which contains data on the largest collection of HNSCC tumor specimens. In this work (8) we found that among patients with HPV negative tumors, reduced survival outcomes associated with tumor protein 53 (TP53) mutation only occur in combination with loss of chromosome 3p. This results in reduction of median survival from 5 years for TP53 mutation to only 1.7 years for ‘double-hit’ mutations (TP53 and 3p) (8). Beyond genetic mutations, the reasons for poor prognoses are still unclear. Current hypotheses focus on decreased radiosensitivity of double-hit tumors and the effects of infiltrating host immune cells (9). Indeed, it has been shown that HNSCC tumors inhibit natural killer cells, T cells and antigen presenting cells while recruiting regulatory T cells and tumor-associated macrophages (TAMs) (6). TAM burden has been shown to be a predictor of lymph node involvement and metastasis and hence tumor aggressiveness (10), and TAMs are known to secrete matrix metalloproteinases (MMP) which promote angiogenesis and tumor progression (11).

To evaluate the role of TAMs in tumors with either TP53 mutation alone (single-hit) or TP53 mutation combined with 3p deletion (double-hit), we identified human HNSCC cell lines (Cal 27, SCC25, SCC15 and SCC4) from the American Type Culture Collection (ATCC) that have differential TP53 status and Fragile Histidine Triad Protein (FHIT) copy number as classified by the Cancer Cell Line Encyclopedia. FHIT, located at position 3p14.2, is the gene locus most highly correlated with the 3p deletion in our TCGA analysis. FHIT is a tumor suppressor gene that has been reported as frequently inactivated in HNSCC cell lines (12). Decreased FHIT expression has been shown to correlate with worse survival in patients with tongue cancer (13). In the 3p region, we found that copy number variation for FHIT correlates best with 3p deletion status. FHIT has been shown to be a tumor suppressor (14), and FHIT deficient mice show both increased incidence of spontaneous tumor formation as well as increased tumor formation in response to carcinogens (15). Interestingly, loss of FHIT expression has been shown to correlate with poor outcomes in patients with tongue cancer (12). Because previous in vivo ratiometric cell penetrating peptide (RACPP) experiments have shown that Cal27 xenografts have higher MMP activity than SCC4

Author Manuscript Author Manuscript Author Manuscript Author Manuscript

xenografts (13), we expect higher TAM accumulation in double-hit Cal27 compared to the single-hit SCC4 xenografts.

Clinically, invasive biopsy is the gold standard for diagnosis and genomic analysis of HNSCC, but there are several disadvantages of biopsying friable tumor tissue adjacent to vital structures in the head and neck which include bleeding, damage to nerves/airway/vessels, tumor cell deposition along the biopsy tract among others (16). Prior work has validated the use of novel fluorine-19 (^{19}F) magnetic resonance imaging (MRI) probe technologies for macrophage tracking in preclinical studies (17-19). In this approach, perfluorocarbon (PFC) nanoemulsion is injected intravenously, and the emulsion droplets are scavenged in situ by cells of the reticuloendothelial system (RES), particularly circulating monocytes, macrophages, neutrophils, and DCs (20). These labeled cells can home to inflammatory foci and can be imaged by ^{19}F MRI with no endogenous background signal. PFC-labeled macrophages dominate MRI-visible ^{19}F “hot-spots” and there is a linear correlation between ^{19}F signal and macrophage burden which can be quantitated directly from the in vivo images (18,21). Our aim is to evaluate this new imaging technology to noninvasively differentiate between double- and single-hit tumors in a rodent model of head and neck tumor xenografts. Our results suggest that in situ PFC macrophage labeling and MRI is an effective non-invasive tool for assaying TAM burden and may be predictive of treatment outcomes and the appropriateness of neoadjuvant treatments.

Methods

HNSCC cell lines

Human tongue squamous cell carcinoma cell lines (Cal27 & SCC4) from ATCC were used. The SCC4 cell line contained a missense TP53 mutation, and the Cal27 cell line contained both FHIT deletion and missense TP53 mutations (4). In detail, this prior work demonstrated homozygous loss of FHIT (FHIT$^{-/-}$) for Cal-27 and FHIT heterozygosity (FHIT$^{+/-}$) for SCC-4. The TP53 gene was mutated in both cell lines; SCC-4 contains a missense mutation (G→A) on nucleotide 7578479 of chromosome 17p, and CAL-27 contains a missense mutation (T→A) on nucleotide 7578271.

Mouse model of HNSCC

Animal protocols were approved by the University of California San Diego Institutional Animal Care and Use Committee (IACUC). Seven-week-old female Fox1^{nu} nude mice (N=10) were obtained from Harlan/Envigo (Indianapolis, IN, USA) and divided into two experimental groups. Five million of either single-hit/ SCC4 or double-hit/Cal27 cells in 50% matrigel (Corning, Tewksbury, MA, USA) and 50% serum free DMEM (Gibco, Waltham, MA, USA) were injected in bilateral lower flanks of mice (N=5 in each group).

PFC emulsion

A sterile and injectable PFC nanoemulsion (VS-1000H, Celsense Inc., PA, USA) was used to label macrophages in situ. The nanoemulsion contains 30% (v/v) perfluoropolyether with a mean droplet size of 145 nm. The ^{19}F magnetic resonance spectrum contains essentially a single major peak, with longitudinal (T_1) and transverse (T_2) relaxation times approximately

Author Manuscript Author Manuscript Author Manuscript Author Manuscript

T_1 /T_2 ~ 450/180 ms at 11.7 Tesla. When PFC is administered intravenously, the nanoemulsion droplets are taken up by cells of the reticuloendothelial system, particularly monocytes and macrophages (22). After visible tumor growth to ~8 mm, as measured by calipers, a single 0.2 ml dose of nanoemulsion (containing approximately 1.2×10^{21} F atoms) was injected intravenously via the lateral tail vein. For histology purposes, one animal in each group received a fluorescent version of the nanoemulsion (VS-1000H-DM-Red, Celsense) containing a bright fluorophore bound to the PFC droplet, with emission/excitation wavelengths equal to 596/615 nm.

In vivo MRI and quantification of ^{19}F signal

Mice were subjected to longitudinal MRI on day 2 and 10 after the PFC injection. The MRI data were acquired using an 11.7 T Bruker BioSpec preclinical scanner (Bruker, Billerica, MA) with a dual-tuned ^{1}H/^{19}F birdcage volume coil (Bruker). During MRI, animals were anesthetized with 2% isoflurane in air, and core temperature was maintained at 37 °C using a heated pad. Reference capillaries with diluted PFC nanoemulsion (5% v/v) in 1% agarose were placed above the animal's torso in the image field of view (FOV). The ^{19}F images were acquired using a RARE (Rapid Acquisition with Relaxation Enhancement) sequence with parameters TR/TE=1250/35 ms, RARE factor 16, matrix 64×64, FOV 30×30 mm^2, slice thickness 1.5 mm, and 8-10 slices. The ^{1}H anatomical images were also acquired using the RARE sequence with TR/TE=1000/18.5 ms, RARE factor 8, matrix 256×256, FOV 30×30 mm^2, and the same slice package as the ^{19}F data. Data were imported into Voxel Tracker® software (Celsense Inc., PA, USA), and ^{19}F regions of interest (ROIs), or hot-spots, were manually outlined with guidance from the anatomical ^{1}H images. ROIs of the ^{19}F reference capillary and background noise were also delineated, where the external ^{19}F capillary was used as an absolute ^{19}F reference, The in vivo ^{19}F signal in ROIs (i.e., apparent ^{19}F atom number) was calculated using Voxel Tracker®, as previously reported (18,23) and quantitative analyses yielded the apparent number of fluorine atoms within the ROIs. For ^{19}F image quantification, full-dynamic range data without thresholding were analyzed. Composite ^{19}F/^{1}H overlay images for display were also created; the ^{19}F images were manually thresholded for visualization purposes to mask noise, and rendered in “red-hot” pseudo-color scale using Fiji software (24), while the ^{1}H image remained in grayscale.

Histology and immunofluorescence

After *in vivo* MRI experiments, tumors and lymph nodes were excised and kept in OCT medium (VWR, Radnor, PA, USA) for histology cryosectioning to evaluate immune cell recruitment. Frozen sections were dried in the dark for 20 min at room temperature, fixed in 4% paraformaldehyde (Affimetrix, Santa Clara, CA) and then incubated with 2.5% BSA in PBS at room temperature for 15 min. Excess blocking reagent was discarded and the slides were incubated overnight in the dark at 4 °C with a rabbit anti-mannose receptor antibody (#64693, Abcam, Cambridge, MA, USA) diluted 1:200 in PBS BSA to bind a receptor present in macrophages. The slides were then washed three times with PBS and incubated for 30 min with Alexa Fluor 488 Goat anti-Rabbit IgG used at 1:200 dilution. Section nuclei were stained with Hoechst (#33342, 1:500 dilution, Thermo Fisher Scientific, Waltham, MA). The slides were washed with PBS three times, mounted using Vectashield (Vector), and photographed in a fluorescence microscope. Confocal images were acquired with a

Author Manuscript Author Manuscript Author Manuscript Author Manuscript

Leica SP5 2 confocal system (Leica Microsystems Inc.) coupled to a Leica DM 6000 CFS microscope and Leica LAS AF 1.8.2 software. Images were acquired using a ×63 immersion objective. Additionally, 5 μm sections (N=3) from six tumors in each group were subjected to immunohistochemistry staining using rabbit polyclonal antibody against CD68 (#125212, Abcam, Cambridge, MA, USA). CD68 stained macrophages were counted with three high power fields (HPF, 40×, N=108) per tumor by a pathologist, and an average macrophage count per tumor was calculated.

Statistics

All measurements are presented as mean ± standard error. A two-tailed T-test with unequal variances was performed to compare groups. The number of macrophages per tumor were correlated with total ^{19}F signal per tumor using a Pearson's correlation coefficient test. P-values <0.05 are considered statistically significant.

Results

In vivo ^{19}F MRI shows macrophage burden in the tumor

In vivo PFC labeling and subsequent ^{1}H/^{19}F MRI revealed several fluorine hotspots located in the abdomen of the mice. The hot-spots are displayed in the periphery of the tumors and in the adjacent lymph nodes (Fig. 1). Visually, there are more hotspots associated with the Cal27 (double-hit) tumors (Fig. 1A and C) versus the SCC4 tumors (single-hit) (Fig. 1B and D).

Quantitatively, ROI analyses reveal that the total number of ^{19}F atoms within the double-hit tumors is twice higher than the SCC4 single-hit tumors two days after PFC delivery (Fig. 2A, P = 0.0034). The difference between the double- and single-hit tumors remains significant at day 10 despite a mild decrease in overall signal over the course of 8 days (p =0.0063), showing that the imaging time window after agent injection is flexible. The number of macrophages per tumor moderately correlated to the fluorine signal (Pearson's r = 0.63, Fig. 2C). These quantitative differences support our hypothesis of increased TAM burden in the double-hit versus single-hit tumors. We also note that proximal lymph nodes (Fig. 1E and F, total 16 lymph nodes in 10 animals, Table 1) display ^{19}F signals adjacent to the tumors, which is consistent with recruited immune cells aggregates within regional draining nodes. Quantitative analysis of the ^{19}F within the lymph nodes show similar amounts of fluorine atoms in both double-hit and single-hit groups at day 2 (average of 3×10^{18} ^{19}F atoms, p = 0.3), which decrease over time (Fig. 2B, p = 0.07) in the double-hit group. The ^{19}F signal within the lymph nodes for both double-hit and single-hit groups are lower than the corresponding tumors by a factor of ~10. At the experimental endpoints, all animals were sacrificed, and the tumors and lymph nodes were excised and cryopreserved for histology.

Ex vivo analyses

Hematoxylin-eosin (H&E) and immunofluorescence staining was performed on cryosectioned tumors and lymph nodes after completion of the MRI experiments (Figs. 3-5). Co-registration of cell nuclei (Hoechst 33342) and macrophage mannose receptor (green)

Author Manuscript Author Manuscript Author Manuscript Author Manuscript

stains enabled qualitative visual assessment of macrophage burden in slide micrographs. The slides reveal the presence of fluorescent green signal in the periphery of both Cal27 double-hit and SCC4 single-hit tumors thus signifying presence of TAMs within tumors (Fig. 4), consistent with the $^{19}F/^{1}H$ MRI observations. The macrophage burden visually appears considerably higher for the Cal27 double-hit tumors (Fig. 4B). Importantly, the dual-mode MRI-fluorescent PFC agent tends to colocalize intracellularly with the green fluorescence depicting TAMs, consistent with macrophage-associated MRI hotspots (Fig. 4C). As expected, similar fluorescence signals are observed in the regional draining lymph nodes (Fig. 5B) confirming the local accumulation of fluorine containing macrophages, compared to a control lymph node showing minimal macrophage presence and no fluorine signal (Fig. 5C).

Discussion

To summarize, we show that PFC nanoemulsion and subsequent $^{1}H/^{19}F$ MRI allows for quantitative assessment of macrophage burden in tumors and adjacent lymph nodes in vivo. This imaging modality enables discrimination between double- and single-hit head and neck cancer xenografts based on differential TAM accumulation at the tumor periphery. These findings are in concordance with histopathologic observations. TAMs have been shown to accumulate at the tumor site and can be detected in vivo using in situ labeling techniques and MRI (25).

Macrophages play a multidimensional role in cancer. TAMs serve several pro-tumoral functions including the expression of growth, angiogenesis and lymphangiogenesis factors. Moreover, TAMs release matrix proteases leading to the suppression of adaptive responses (26,27). Considering this, the ^{19}F hotspots possibly represent the colonizing front of the tumor. M1 macrophage subtype demonstrate high capacity to present antigens and activate polarized type I T-cell responses resulting in cytotoxicity towards tumor cells. On the other hand, M2 macrophages have poor antigen presenting capacity, suppress inflammatory responses and Th1 adaptive immunity and thus contribute in hijacking the local immune system away from anti-tumor function (28). Tissue-resident macrophage number may be amplified through the recruitment and differentiation of circulating monocytes in the context of inflammation/tumor expansion (29). Many growth and differentiation factors like M-CSF, PGE2, IL-6 & IL-10 expressed in the tumor microenvironment have the potential to promote differentiation and polarization of recruited monocytes into TAMs of the M2 subtype (30). TAMs also exert immunosuppressive activity by releasing chemokines that preferentially attract T-cell subsets devoid of cytotoxic function and thus facilitate tumor progression and metastatic invasion (5). In situ labeling of TAMs with PFC does not permit M1/M2 phenotype discrimination.

Our results show increased accumulation of TAMs within the Cal27 double-hit tumors compared to the SCC4 single-hit tumors, thus confirming prior work that higher frequency of infiltrating TAM has been associated with poor prognosis in many human tumors particularly lymphoma, liver and breast cancers (26,31-33). These preliminary preclinical observations could potentially have significant clinical relevance. Prior work has shown double-hit HNSCC is less radiosensitive compared to single-hit tumors; the increased TAM

Author Manuscript Author Manuscript Author Manuscript Author Manuscript

accumulation in double-hit tumors could partially explain the observed aggressiveness (13). Patients with double-hit/more aggressive tumor genotype would not benefit from radiotherapy alone, thus different treatment options would be preferred that lead to increased survival, such as conjunction of radiotherapy with chemotherapy or inhibitors of the radioresistance pathway (34,35). Conversely, lower grade single-hit tumor patients could be steered toward radiotherapy and/or surgical resection (35,36).

In vivo ^{19}F MRI also revealed high signal in local lymph nodes adjacent to both double-hit and single-hit tumors. Overall, signals in the lymph nodes were ten times lower than in the tumors. Histopathologic analyses further confirmed the presence of fluorine-labeled macrophages within these lymph nodes, compared to control lymph nodes from naïve mice which showed minimal macrophage presence. In situ PFC cell labeling is expected to only label a small portion of macrophages. Go et al. (5) reported similar results for gastric cancer, describing immune cell accumulation in the lymphatic vessels of metastatic lymph nodes. They hypothesized that TAMs induce lymphangiogenesis and enhance lymphatic spreading of cancer by secreting vascular endothelial growth factor (VEGF-C) (5). They also noted that the number of intranodal immune cells in non-metastatic nodes was higher in regions nearest to primary tumor, suggesting migration of macrophages from primary tumor to augment intranodal lymphangiogenesis (5). In addition, the chemokines produced by TAMs in the tumor may reach the draining lymph nodes, and thus the tumor may thereby change the microenvironment of the surrounding regional lymph nodes before colonization of tumor cells. Others have shown that the density of M2 macrophages in regional lymph nodes is associated with lymphangiogenesis and occult nodal metastasis of pancreatic, oral squamous cell and esophageal cancers (37,38). This would imply that the high ^{19}F signals we observe adjacent to the tumors are regional lymph nodes. Since these ^{19}F MRI-visible regional nodes indicate both local macrophage accumulation and potential spread of tumor, this information could be used for surgical planning to noninvasively map the regional draining lymph nodes associated with the tumor if these imaging techniques could be translated to humans, as discussed below.

Overall, using nanoparticulate imaging probes, there are two hypotheses regarding the in vivo sites for TAM labeling (39); the first includes extravasation of circulating probe through the leaky tumoral vessels which is then scavenged by local TAMs (40,41). The second hypothesis (42) suggests that reticuloendothelial cells, particularly monocytes, are labeled in the peripheral blood, which then migrate to the site of the cancer to serve a role of immune modulatory cells (29,39) We note that the plasma half-life of the PFC nanoemulsion formulation used is ~9.5 hours in rodents (23); thus, there is ample time for either (or both) hypothesis(es) to be relevant. Our view is that the actual in vivo site where labeling occurs is not central to the interpretation of the ^{19}F image data.

The ^{19}F hotspots observed in this study were most likely dominated by labeled macrophages, but it is possible that other cells contributed to the observed ^{19}F signal. Very small numbers of B lymphocytes, neutrophils, and dendritic cells will take up PFC nanoemulsion (42,43). Measuring the average amount of PFC uptake per cell (macrophage) in situ is not feasible, unlike the case of ex vivo labeling experiments, where apparent cell numbers at hotspots can be directly deduced from the in vivo imaging data after labeled cell

Author Manuscript Author Manuscript Author Manuscript Author Manuscript

infusion (44,45). However, it has previously been shown (18,21) that the apparent number of ^{19}F atoms detected linearly correlates to the number of macrophages present and the inflammatory burden in vivo. Thus, relative TAM burden comparisons between tumors of different genotypes based on ^{19}F atom counts is plausible. Generally, MRI-detectable macrophages labeled with PFC can persist for long time periods; for example, a recent study using the same imaging agent in a murine model of inflammatory bowel disease (46) displayed PFC-labeled macrophages in the bowel wall for 110 days. Over time, eventually the PFC enters the RES system, particularly Kupffer cells of the liver, and PFC slowly clears the body via lung exhalation (47,48).

Our results suggest that there is a clinical rationale for potentially developing ^{19}F inflammation imaging for clinical diagnostic use. The PFC agent used in these studies was for preclinical use only, and there are currently no approved PFC agents for clinical inflammation imaging. However, we note that a PFC imaging agent with a similar composition to what has been used here has been employed in a first-in-man clinical trial to detect immunotherapeutic dendritic cell vaccines injected into colorectal cancer patients (49). However, in this study, a minuscule dose is delivered to the patient compared to what is needed for in situ cell labeling as described here, thus the clinical development pathway is more complex. Also, there are potential adverse effects of large PFC emulsion doses as observed in artificial blood substitute studies; side effects included headache, dizziness, nausea, vomiting, back and chest pain, but these were mostly mild (79.8% of patients) (50); moreover, the severity of these effects may be dependent upon the choice of molecular components for PFC nanoemulsion formulation.

The notion of performing ^{19}F MRI has been around for at least 40 years (51). Certainly, technical barriers associated with implementation of ^{19}F MRI on a clinical scanner are surmountable, as the resonant frequency of ^{19}F differs from ^{1}H by only ~6%. Many current generations of clinical scanners can be adapted to detect ^{19}F, with minor hardware/software modifications (45). The sensitivity loss for the detection of labeled TAMs at lower clinical field strengths (3 T) compared to the preclinical MRI scanner (11.7 T) used in this study will depend on multiple factors such as field strength, coil configuration, voxel size and pulse sequence used, amongst other factors (52). One of the rate limiting factors in the clinical adoption of ^{19}F-based technologies is the current availability of ^{19}F-capable scanners in a hospital setting.

Conclusions

To conclude, we demonstrate the use of a novel non-invasive method to quantify apparent macrophage burden within head and neck tumors and local lymph nodes based on the use of PFC nanoemulsions and ^{19}F MRI detection. We show that this technology can discriminate between single- and double-hit tumors with characteristic macrophage burden patterns, as well as sentinel lymph node involvement. Such an imaging tool would be very beneficial in a clinical setting to tailor personalized therapy without unnecessary biopsies.

Author Manuscript Author Manuscript Author Manuscript Author Manuscript

Acknowledgments

We thank Monica Valeria Estrada for histopathology assistance. This work was funded by the National Institutes of Health grants R01-EB017271, R01-134633, 1TL1 TR001443 and the California Institute for Regenerative Medicine grant LA1-C12-06919. E.T.A is a Founder, member of the scientific advisory board and shareholder at Celsense, Inc.

References

1. Ferlay J, Shin HR, Bray F, Forman D, Mathers C, Parkin DM. Estimates of worldwide burden of cancer in 2008: GLOBOCAN 2008. Int J Cancer. 2010; 127(12):2893–2917. [PubMed: 21351269]
2. Sanderson RJ, Ironside JA. Squamous cell carcinomas of the head and neck. BMJ. 2002; 325(7368): 822–827. [PubMed: 12376446]
3. Edge SB, Compton CC. The American Joint Committee on Cancer: the 7th edition of the AJCC cancer staging manual and the future of TNM. Ann Surg Oncol. 2010; 17(6):1471–1474. [PubMed: 20180029]
4. Saber CN, Gronhoj Larsen C, Dalianis T, von Buchwald C. Immune cells and prognosis in HPV-associated oropharyngeal squamous cell carcinomas: Review of the literature. Oral Oncol. 2016; 58:8–13. [PubMed: 27311396]
5. Go Y, Tanaka H, Tokumoto M, Sakurai K, Toyokawa T, Kubo N, Muguruma K, Maeda K, Ohira M, Hirakawa K. Tumor-associated macrophages extend along lymphatic flow in the pre-metastatic lymph nodes of human gastric cancer. Ann Surg Oncol. 2016; 23(2):S230–235. [PubMed: 25743331]
6. Russell S, Angell T, Lechner M, Liebertz D, Correa A, Sinha U, Kokot N, Epstein A. Immune cell infiltration patterns and survival in head and neck squamous cell carcinoma. Head Neck Oncol. 2013; 5(3):24. [PubMed: 24723971]
7. Cancer Genome Atlas N. Comprehensive genomic characterization of head and neck squamous cell carcinomas. Nature. 2015; 517(7536):576–582. [PubMed: 25631445]
8. Gross AM, Orosco RK, Shen JP, Egloff AM, Carter H, Hofree M, Choueiri M, Coffey CS, Lippman SM, Hayes DN, et al. Multi-tiered genomic analysis of head and neck cancer ties TP53 mutation to 3p loss. Nat Genet. 2014; 46(9):939–943. [PubMed: 25086664]
9. Hu B, Han SY, Wang X, Ottey M, Potoczek MB, Dicker A, Huebner K, Wang Y. Involvement of the Fhit gene in the ionizing radiation-activated ATR/CHK1 pathway. J Cell Physiol. 2005; 202(2):518–523. [PubMed: 15389587]
10. Koontongkaew S. The tumor microenvironment contribution to development, growth, invasion and metastasis of head and neck squamous cell carcinomas. J Cancer. 2013; 4(1):66–83. [PubMed: 23386906]
11. Kang JC, Chen JS, Lee CH, Chang JJ, Shieh YS. Intratumoral macrophage counts correlate with tumor progression in colorectal cancer. J Surg Oncol. 2010; 102(3):242–248. [PubMed: 20740582]
12. Lee JI, Soria JC, Hassan K, Liu D, Tang X, El-Naggar A, Hong WK, Mao L. Loss of Fhit expression is a predictor of poor outcome in tongue cancer. Cancer Res. 2001; 61(3):837–841. [PubMed: 11221865]
13. Raju SC, Hauff SJ, Lemieux AJ, Orosco RK, Gross AM, Nguyen LT, Savariar E, Moss W, Whitney M, Cohen EE, et al. Combined TP53 mutation/3p loss correlates with decreased radiosensitivity and increased matrix-metalloproteinase activity in head and neck carcinoma. Oral Oncol. 2015; 51(5):470–475. [PubMed: 25735654]
14. Ohta M, Inoue H, Cotticelli MG, Kastury K, Baffa R, Palazzo J, Siprashvili Z, Mori M, McCue P, Druck T, et al. The FHIT gene, spanning the chromosome 3p14.2 fragile site and renal carcinoma-associated t(3;8) breakpoint, is abnormal in digestive tract cancers. Cell. 1996; 84(4):587–597. [PubMed: 8598045]
15. Zanesi N, Fidanza V, Fong LY, Mancini R, Druck T, Valtieri M, Rudiger T, McCue PA, Croce CM, Huebner K. The tumor spectrum in FHIT-deficient mice. Proc Natl Acad Sci U S A. 2001; 98(18): 10250–10255. [PubMed: 11517343]

Author Manuscript Author Manuscript Author Manuscript Author Manuscript

16. Oetter N, Knipfer C, Rohde M, von Wilmowsky C, Maier A, Brunner K, Adler W, Neukam FW, Neumann H, Stelzle F. Development and validation of a classification and scoring system for the diagnosis of oral squamous cell carcinomas through confocal laser endomicroscopy. J Transl Med. 2016; 14(1):159. [PubMed: 27255924]
17. Flogel U, Su S, Kreideweiss I, Ding Z, Galbarz L, Fu J, Jacoby C, Witzke O, Schrader J. Noninvasive detection of graft rejection by in vivo (19) F MRI in the early stage. Am J Transplant. 2011; 11(2):235–244. [PubMed: 21214858]
18. Kadayakkara DK, Ranganathan S, Young WB, Ahrens ET. Assaying macrophage activity in a murine model of inflammatory bowel disease using fluorine-19 MRI. Laboratory Investigation. 2012; 92(4):636–645. [PubMed: 22330343]
19. Zhong J, Narsinh K, Morel PA, Xu H, Ahrens ET. In vivo quantification of inflammation in experimental autoimmune encephalomyelitis rats using fluorine-19 magnetic resonance imaging reveals immune cell recruitment outside the nervous system. PLoS One. 2015; 10(10):e0140238. [PubMed: 26485716]
20. Flaim SF. Pharmacokinetics and side effects of perfluorocarbon-based blood substitutes. Artif Cells Blood Substit Immobil Biotechnol. 1994; 22(4):1043–1054. [PubMed: 7849908]
21. Ahrens ET, Young WB, Xu H, Pusateri LK. Rapid quantification of inflammation in tissue samples using perfluorocarbon emulsion and fluorine-19 nuclear magnetic resonance. BioTechniques. 2011; 50(4):229–234. [PubMed: 21548906]
22. Jacoby C, Temme S, Mayenfels F, Benoit N, Krafft MP, Schubert R, Schrader J, Flogel U. Probing different perfluorocarbons for in vivo inflammation imaging by 19F MRI: image reconstruction, biological half-lives and sensitivity. NMR Biomed. 2014; 27(3):261–271. [PubMed: 24353148]
23. Hitchens TK, Ye Q, Eytan DF, Janjic JM, Ahrens ET, Ho C. F-19 MRI Detection of Acute Allograft Rejection with In Vivo Perfluorocarbon Labeling of Immune Cells. Magn Reson Med. 2011; 65(4):1145–1154.
24. Schindelin J, Arganda-Carreras I, Frise E, Kaynig V, Longair M, Pietzsch T, Preibisch S, Rueden C, Saalfeld S, Schmid B, et al. Fiji: an open-source platform for biological-image analysis. Nat Methods. 2012; 9(7):676–682. [PubMed: 22743772]
25. Daldrup-Link HE, Golovko D, Ruffell B, Denardo DG, Castaneda R, Ansari C, Rao J, Tikhomirov GA, Wendland MF, Corot C, et al. MRI of tumor-associated macrophages with clinically applicable iron oxide nanoparticles. Clin Cancer Res. 2011; 17(17):5695–5704. [PubMed: 21791632]
26. Balkwill F, Charles KA, Mantovani A. Smoldering and polarized inflammation in the initiation and promotion of malignant disease. Cancer Cell. 2005; 7(3):211–217. [PubMed: 15766659]
27. Pollard JW. Tumour-educated macrophages promote tumour progression and metastasis. Nat Rev Cancer. 2004; 4(1):71–78. [PubMed: 14708027]
28. Gordon S, Taylor PR. Monocyte and macrophage heterogeneity. Nat Rev Immunol. 2005; 5(12): 953–964. [PubMed: 16322748]
29. Williams CB, Yeh ES, Soloff AC. Tumor-associated macrophages: unwitting accomplices in breast cancer malignancy. NPJ Breast Cancer. 2016; 2
30. Mantovani A, Sozzani S, Locati M, Allavena P, Sica A. Macrophage polarization: tumor-associated macrophages as a paradigm for polarized M2 mononuclear phagocytes. Trends Immunol. 2002; 23(11):549–555. [PubMed: 12401408]
31. Budhu A, Forgues M, Ye QH, Jia HL, He P, Zanetti KA, Kammula US, Chen Y, Qin LX, Tang ZY, et al. Prediction of venous metastases, recurrence, and prognosis in hepatocellular carcinoma based on a unique immune response signature of the liver microenvironment. Cancer Cell. 2006; 10(2):99–111. [PubMed: 16904609]
32. Dave SS, Wright G, Tan B, Rosenwald A, Gascoyne RD, Chan WC, Fisher RI, Braziel RM, Rimsza LM, Grogan TM, et al. Prediction of survival in follicular lymphoma based on molecular features of tumor-infiltrating immune cells. N Engl J Med. 2004; 351(21):2159–2169. [PubMed: 15548776]
33. Paik S, Shak S, Tang G, Kim C, Baker J, Cronin M, Baehner FL, Walker MG, Watson D, Park T, et al. A multigene assay to predict recurrence of tamoxifen-treated, node-negative breast cancer. N Engl J Med. 2004; 351(27):2817–2826. [PubMed: 15591335]

Author Manuscript Author Manuscript Author Manuscript Author Manuscript

34. Perri F, Pacelli R, Della Vittoria Scarpati G, Cella L, Giuliano M, Caponigro F, Pepe S. Radioresistance in head and neck squamous cell carcinoma: biological bases and therapeutic implications. Head Neck. 2015; 37(5):763–770. [PubMed: 24995469]
35. Suh Y, Amelio I, Guerrero Urbano T, Tavassoli M. Clinical update on cancer: molecular oncology of head and neck cancer. Cell Death Dis. 2014; 5:e1018. [PubMed: 24457962]
36. Corvo R. Evidence-based radiation oncology in head and neck squamous cell carcinoma. Radiother Oncol. 2007; 85(1):156–170. [PubMed: 17482300]
37. Kurahara H, Takao S, Maemura K, Mataki Y, Kuwahata T, Maeda K, Sakoda M, Iino S, Ishigami S, Ueno S, et al. M2-polarized tumor-associated macrophage infiltration of regional lymph nodes is associated with nodal lymphangiogenesis and occult nodal involvement in pN0 pancreatic cancer. Pancreas. 2013; 42(1):155–159. [PubMed: 22699204]
38. Wehrhan F, Buttner-Herold M, Hyckel P, Moebius P, Preidl R, Distel L, Ries J, Amann K, Schmitt C, Neukam FW, et al. Increased malignancy of oral squamous cell carcinomas (oscc) is associated with macrophage polarization in regional lymph nodes - an immunohistochemical study. BMC Cancer. 2014; 14:522. [PubMed: 25042135]
39. Corot C, Robert P, Idee JM, Port M. Recent advances in iron oxide nanocrystal technology for medical imaging. Adv Drug Deliv Rev. 2006; 58(14):1471–1504. [PubMed: 17116343]
40. Baxter LT, Jain RK. Transport of fluid and macromolecules in tumors. I. Role of interstitial pressure and convection. Microvasc Res. 1989; 37(1):77–104. [PubMed: 2646512]
41. Mason RP, Antich PP, Babcock EE, Constantinescu A, Peschke P, Hahn EW. Non-invasive determination of tumor oxygen tension and local variation with growth. Int J Radiat Oncol Biol Phys. 1994; 29(1):95–103. [PubMed: 8175452]
42. Flogel U, Ding Z, Hardung H, Jander S, Reichmann G, Jacoby C, Schubert R, Schrader J. In vivo monitoring of inflammation after cardiac and cerebral ischemia by fluorine magnetic resonance imaging. Circulation. 2008; 118(2):140–148. [PubMed: 18574049]
43. Hertlein T, Sturm V, Kircher S, Basse-Lusebrink T, Haddad D, Ohlsen K, Jakob P. Visualization of abscess formation in a murine thigh infection model of staphylococcus aureus by F-19-magnetic resonance imaging (MRI). Plos One. 2011; 6(3)
44. Srinivas M, Morel PA, Ernst LA, Laidlaw DH, Ahrens ET. Fluorine-19 MRI for visualization and quantification of cell migration in a diabetes model. Magn Reson Med. 2007; 58(4):725–734. [PubMed: 17899609]
45. Ahrens ET, Zhong J. In vivo MRI cell tracking using perfluorocarbon probes and fluorine-19 detection. NMR Biomed. 2013; 26(7):860–871. [PubMed: 23606473]
46. Shin SH, Kadayakkara DK, Bulte JW. In vivo 19F MR imaging cell tracking of inflammatory macrophages and site-specific development of colitis-associated dysplasia. Radiology. 2017; 282(1):194–201. [PubMed: 27440581]
47. Lowe KC. Engineering blood: Synthetic substitutes from fluorinated compounds. Tissue Eng. 2003; 9(3):389–399. [PubMed: 12857407]
48. Riess JG. Understanding the fundamentals of perfluorocarbons and perfluorocarbon emulsions relevant to in vivo oxygen delivery. Artif Cells Blood Substit Immobil Biotechnol. 2005; 33(1):47–63. [PubMed: 15768565]
49. Ahrens ET, Helfer BM, O'Hanlon CF, Schirda C. Clinical cell therapy imaging using a perfluorocarbon tracer and fluorine-19 MRI. Magn Reson Med. 2014; 72(6):1696–1701. [PubMed: 25241945]
50. Noveck RJ, Shannon EJ, Leese PT, Shorr JS, Flaim KE, Keipert PE, Woods CM. Randomized safety studies of intravenous perflubron emulsion. II. Effects on immune function in healthy volunteers. Anesth Analg. 2000; 91(4):812–822. [PubMed: 11004031]
51. Holland GN, Bottomley PA, Hinshaw WS. 19F magnetic resonance imaging. J Magn Reson. 1977; 28(1):133–136.
52. Hashemi RH, Bradley WG. MRI the basics. LW & W. 1997

Author Manuscript Author Manuscript Author Manuscript Author Manuscript

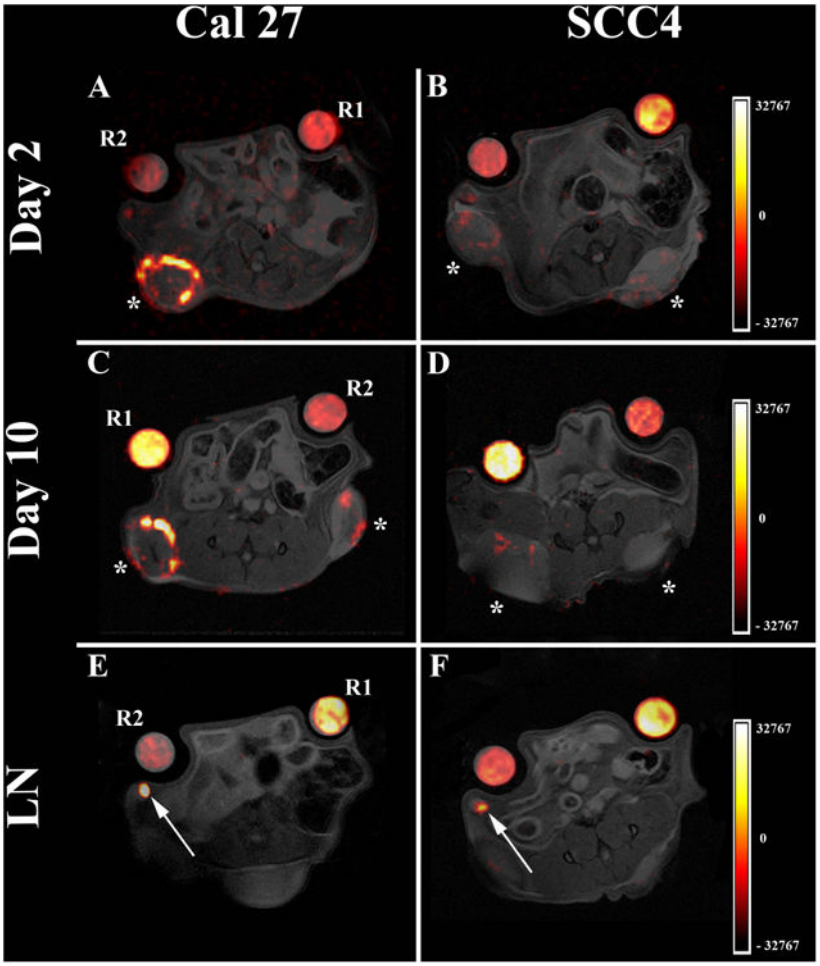

Figure 1.

In vivo MRI displaying PFC distribution in the tumor periphery and draining lymph nodes. A. and C. Representative $^{1}H/^{19}F$ pseudo-color overlays of a mouse bearing Cal27 tumors showing significant macrophage infiltrates in the periphery of the tumors at day 2 and 10 respectively. B. and D. Representative $^{1}H/^{19}F$ overlays of a mouse bearing SCC4 tumors showing decreased macrophage burden at day 2 and 10 post PFC injection. E. and F. Corresponding $^{1}H/^{19}F$ pseudo-color overlays demonstrating fluorine hotspots (arrows) within local lymph nodes (LN) of the same animals in both Cal27 (E.) and SCC4 groups (F.). Tumors and lymph nodes were not visible in the same axial plane and therefore alternate slices were selected to show lymph node hotspots. Asterisks indicate the implanted tumors; R1 and R2 indicate tubes for reference quantification and the color scale is in arbitrary units.

Author Manuscript Author Manuscript Author Manuscript Author Manuscript

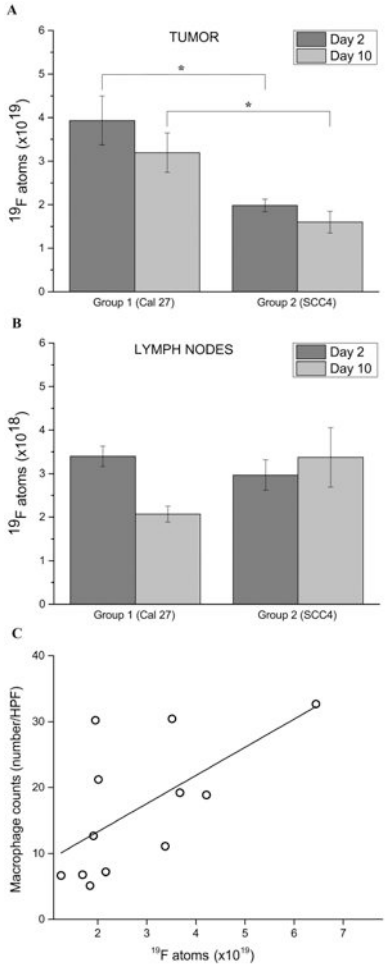

Figure 2.

Quantitative analysis of macrophage burden in the tumors and draining lymph nodes from in vivo MRI data. A. ^{19}F atom count is significantly higher in Cal27 tumors compared to SCC4 tumors at both time points (day 2 & 10 post PFC injection, asterisk indicates significance); this count is almost twice as high 2 days after PFC injection (3.94×10^{19} versus 1.98×10^{19} atoms respectively, $p = 0.0034$). B. Corresponding ^{19}F atom count in the draining lymph nodes showing minor signal decrease for Cal27 tumors at day 10 compared to day 2 but no difference between the two groups at day 2; these differences were not significant, $p>0.05$. Overall, signal in the lymph nodes is lower than in the periphery of the corresponding tumors by a factor of ~10. C. Plot showing moderate correlation ($r = 0.63$) between number of fluorine atoms per tumor and macrophage infiltration (N=108, high power fields, HPF).

Author Manuscript Author Manuscript Author Manuscript Author Manuscript

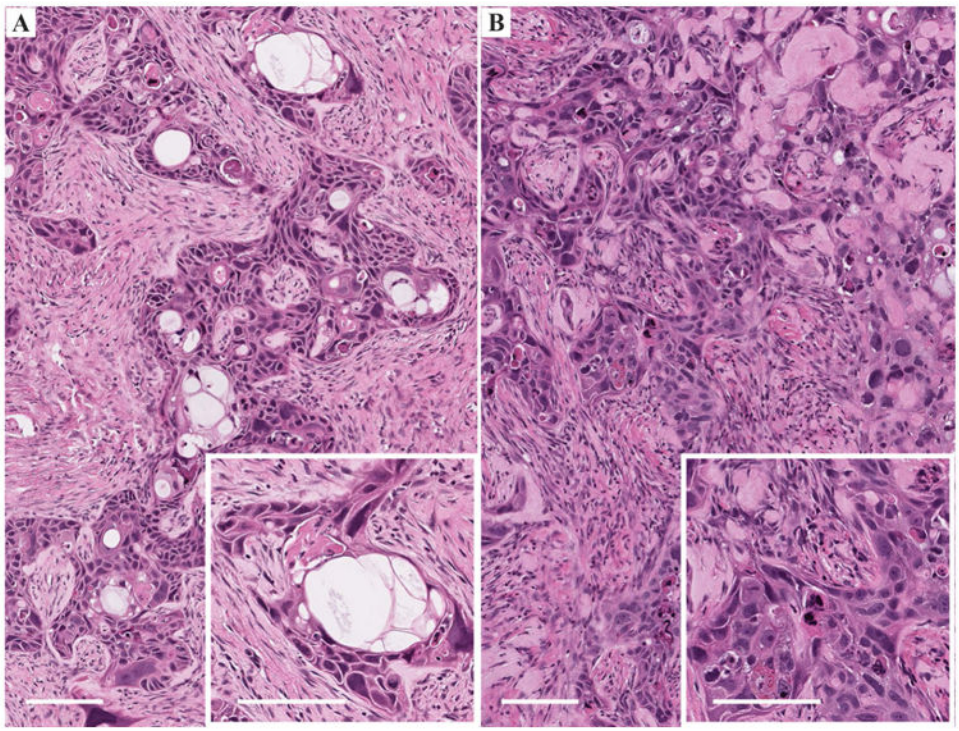

Figure 3.

Histopathologic analyses of excised tumors stained with H&E. A. Moderately differentiated squamous cell carcinoma infiltrating a dense fibroblastic stroma. Numerous pseudocystic structures (white spaces) can be seen characteristic of this squamous cell carcinoma cell line. The inset shows a hyperintense multilocular structure containing cell debris. The proliferating cells are quite abnormal, depicting irregularly shaped and hyperchromatic nuclei. Bars represent 100 μm. B. Moderate to poorly differentiated squamous cell carcinoma infiltrating a hyalinized fibroblastic stroma. Squamous differentiation is focal. The inset shows the atypicity of the proliferating cells and the absence of clear keratinization. Bars represent 100 μm.

Author Manuscript Author Manuscript Author Manuscript Author Manuscript

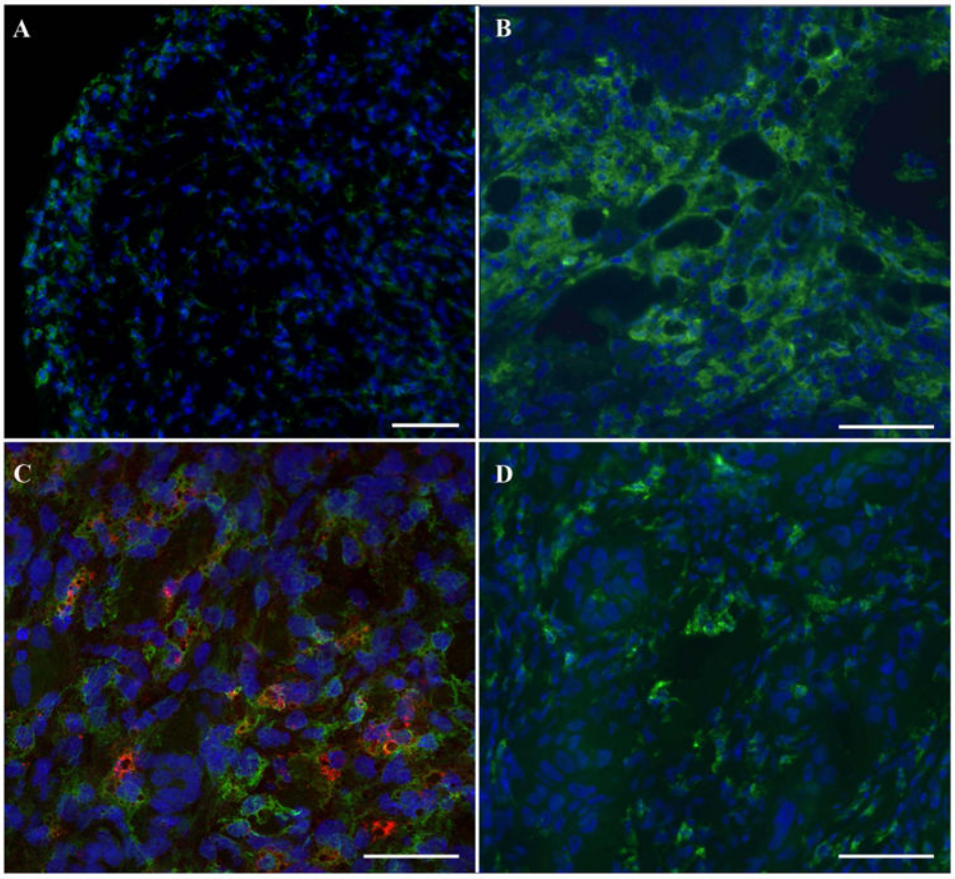

Figure 4.

Immunofluorescence images of excised tumors. A. Low magnification immunofluorescence staining displays green fluorescent signal from TAMs (anti-mannose receptor, green), which confirming accumulation in the periphery of the tumors, and is consistent with the ^{19}F MRI (Fig. 1). Scale bar is 100 μm. B. Qualitatively, numerous macrophages are observed within Cal27 tissue samples. C. Shows composite image of fluorescent dual-mode PFC (VS-1000H-DM Red) and macrophage (anti-mannose receptor, green) immunostaining and demonstrates intracellular uptake of PFC agent by macrophages in a Cal27 tissue sample. D. SCC4 tissue stains show scattered macrophages. Nuclei are stained with blue Hoechst 33342 stain. Scale bars (B-D) = 25 μm.

Author Manuscript Author Manuscript Author Manuscript Author Manuscript

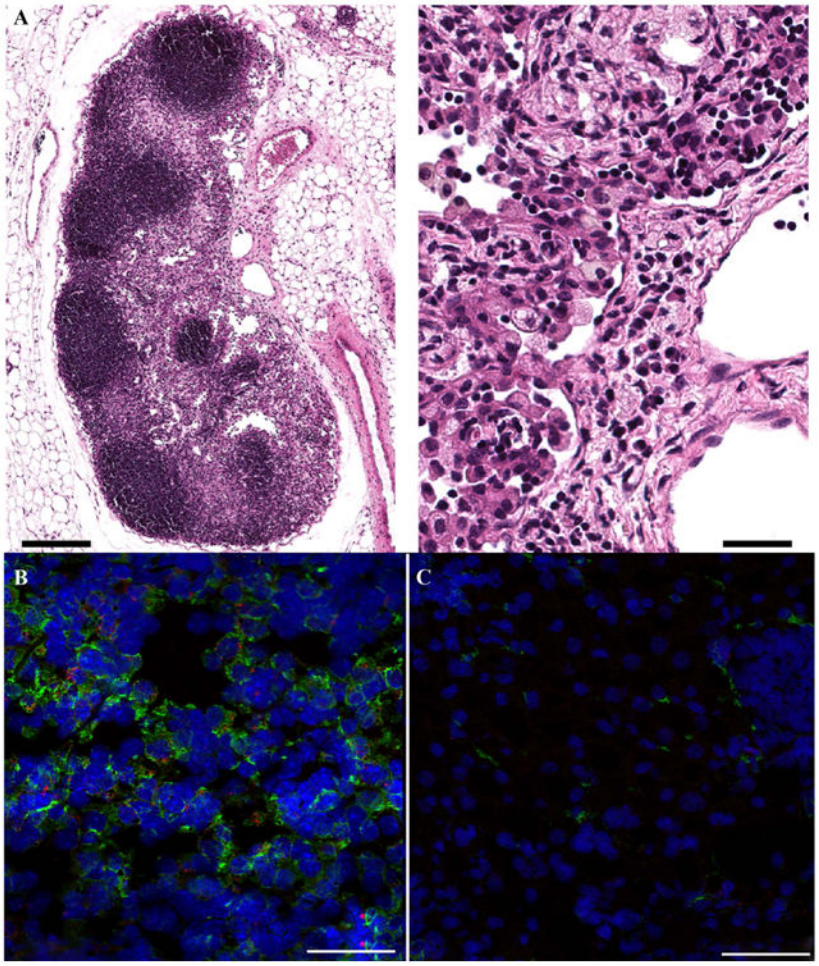

Figure 5.

Histopathologic images of excised lymph nodes. A. H&E staining demonstrates numerous foamy macrophages within the excised lymph nodes. Left and right scale bars are 200 and 20 μm, respectively. B. Immunofluorescence staining demonstrates colocalization of macrophages (green) and intracellular dual-mode PFC (VS-1000H-DM Red) in lymph node, consistent with MRI findings (Fig. 1). Scale bar = 50 μm. Control lymph node in (C) displays minimal macrophage presence and an absence of PFC label. Scale bar = 50 μm.

Author Manuscript

Author Manuscript

Author Manuscript

Author Manuscript

Table 1

Fluorine positive lymph nodes at Day 10. This table enumerates the number of individual (local & retroperitoneal) lymph nodes which demonstrated fluorine hot spots for both double hit (Cal 27) and single hit (SCC 4) groups 10 days post IV perfluorocarbon injection.

Lymph nodes at Day 10			
	Local LN	**Retroperitoneal LN**	
Cal 27_Ml	0	0	
Cal 27_M2	2	0	
Cal 27_M3	2	0	
Cal 27_M4	0	2	
Cal 27_M5	2	0	
SCC4_M1	1 (R)	0	
SCC4_M2	1 (R)	2	
SCC4_M3	1 (R)	1 (L)	
SCC4_M4	1 (R)	0	
SCC4M5	1 (R)	0	
		LEGEND	
		2	Bilateral
		1 (R) or 1 (L)	Unilateral right or left
		0	None